Journal of
Materials Chemistry C

PAPER

Cite this: J. Mater. Chem. C, 2015, 3, 8200

Nano surface engineering of Mn_2O_3 for potential light-harvesting application

Prasenjit Kar,[a] Samim Sardar,[a] Srabanti Ghosh,[a] Manas R. Parida,[b] Bo Liu,[c] Omar F. Mohammed,[b] Peter Lemmens[cd] and Samir Kumar Pal*[a]

Received 22nd May 2015,
Accepted 5th July 2015

DOI: 10.1039/c5tc01475a

www.rsc.org/MaterialsC

Manganese oxides are well known applied materials including their use as efficient catalysts for various environmental applications. Multiple oxidation states and their change due to various experimental conditions are concluded to be responsible for their multifaceted functionality. Here we demonstrate that the interaction of a small organic ligand with one of the oxide varieties induces completely new optical properties and functionalities (photocatalysis). We have synthesized Mn_2O_3 microspheres *via* a hydrothermal route and characterized them using scanning electron microscopy (SEM), X-ray diffraction (XRD) and elemental mapping (EDAX). When the microspheres are allowed to interact with the biologically important small ligand citrate, nanometer-sized surface functionalized Mn_2O_3 (NPs) are formed. Raman and Fourier transformed infrared spectroscopy confirm the covalent attachment of the citrate ligand to the dangling bond of Mn at the material surface. While cyclic voltammetry (CV) and X-ray photoelectron spectroscopy (XPS) analysis confirm multiple surface charge states after the citrate functionalization of the Mn_2O_3 NPs, new optical properties of the surface engineered nanomaterials in terms of absorption and emission emerge consequently. The engineered material offers a novel photocatalytic functionality to the model water contaminant methylene blue (MB). The effect of doping other metal ions including Fe^{3+} and Cu^{2+} on the optical and catalytic properties is also investigated. In order to prepare a prototype for potential environmental application of water decontamination, we have synthesized and duly functionalized the material on the extended surface of a stainless steel metal mesh (size 2 cm × 1.5 cm, pore size 150 μm × 200 μm). We demonstrate that the functionalized mesh always works as a "physical" filter of suspended particulates. However, it works as a "chemical" filter (photocatalyst) for the potential water soluble contaminant (MB) in the presence of solar light.

1. Introduction

The beauty of nanomaterials lies in their higher surface to volume ratio compared to that of the bulk material with the same chemical composition. Therefore, for tailor made applications, nanomaterials are more promising compared to their bulk counterpart. In addition, to be used in several practical applications further surface modifications of nanomaterials are essential.[1–5] Attaching suitable organic ligands to their surface atoms is one of the most facile route for modification of metal oxide nanomaterials.[6] This leads, *e.g.* to protection of nanoparticles (NPs) from agglomeration and makes them available for an interaction with other molecules. Frequent reports on functionalization of NPs with biocompatible ligands for catalysis, cancer therapy and biomedical applications exist.[7–11] Previously, our group functionalized various NPs with biologically important ligands to allow potential biomedical and environmental applications.[12–15] Our recent attention towards manganese oxide NPs is due to their emerging use in biomedical, photocatalysis, supercapacitor applications and also because this material is relatively inexpensive, non-toxic, and naturally abundant.[16–20] It has been reported that different varieties of manganese oxide NPs (MnO, Mn_2O_3, Mn_3O_4) with tunable morphologies can be easily synthesized *via* different routes.[21–25] By varying the dripping speed of NaOH in the presence of $MnCl_2$ and H_2O_2, different Mn_3O_4 morphologies, like nanoparticles, nanorods and nanofractals can be obtained.[26,27] While hollow and core shell type Mn_2O_3 nanostructures are applied in CO reduction,[28] the former are reported to be useful in pollutant adsorption.[29] Recently, Chen *et al.* have shown that

[a] Department of Chemical, Biological and Macromolecular Sciences, S. N. Bose National Centre for Basic Sciences, Block JD, Sector III, SaltLake, Kolkata 700 098, India. E-mail: skpal@bose.res.in
[b] Solar and Photovoltaics Engineering Research Center, Division of Physical Sciences and Engineering, King Abdullah University of Science and Technology, Thuwal 23955-6900, Saudi Arabia
[c] Institute for Condensed Matter Physics, TU Braunschweig, Mendelssohnstraße 3, 38106 Braunschweig, Germany
[d] Laboratory for Emerging Nanometrology, TU Braunschweig, Braunschweig, Germany

hierarchical mesoporous manganese dioxide (MnO_2) synthesized by a soft interface method is a much efficient catalyst for degradation of organic pollutants like methylene blue.[30] To make the low band gap material Mn_2O_3 photocatalytically active a contact between graphene sheets and Mn_2O_3 nanoparticles has been made to facilitate easy electron transfer from the metal oxide to the graphene sheet.[31] Functionalized manganese oxide NPs are also reported to have novel optical and catalytic properties.[3] In recent reports from our group we have shown that the interaction of Mn_3O_4 NPs with various hydroxyl and carboxylate containing ligands changes the optical and magnetic properties of the NPs.[32] While α-hydroxy-carboxylate is found to have an impact on the optical properties of the NPs through ligand to metal charge transfer (LMCT) and Jahn–Teller effects, interaction with carboxyl containing ligands is efficient in controlling the magnetic properties of Mn_3O_4 NPs.[32] Citrate functionalized Mn_3O_4 NPs containing multiple oxidation states (+2, +3 and +4) have been recently found to be useful for the treatment of hyperbilirubinemia.[13] The balance of different oxidation states in functionalized NPs is critical to achieve novel optical and catalytic properties. In this context, the functionalization of Mn_2O_3 having only one oxidation state (+3) and inducing interesting optical properties would be important, however, this is only sparsely reported in the literature. This is one of the motives of the present work. Another important aspect is doping of Mn_2O_3 with metal ions in order to improve the functionality of the native oxide. Patoux *et al.* have shown that nickel doped spinel manganese oxides are attractive materials for Li ion batteries.[33] Zinc doped manganese oxides are efficient coal gas absorbers for desulfurization.[34] Recently, Fe-loaded mesoporous manganese dioxide with urchin-like superstructures have been successfully used for dye degradation.[35] Therefore, we have also investigated the optical and catalytic properties of doped Mn_2O_3 upon functionalization with organic ligands.

In this work, we have synthesized Mn_2O_3 microspheres by a hydrothermal process and duly functionalized them with the model organic ligand citrate. High resolution transmission electron microscopy (HRTEM) reveals the formation of Mn_2O_3 nanoparticles (NPs) from the microsphere as a result of ligand etching.[36,37] We further confirmed the nature of citrate binding to the NPs by a series of characterization techniques such as Raman scattering, Fourier transformed infrared (FTIR) spectroscopy, cyclic voltammetry (CV) and X-ray photo-emission spectroscopy (XPS). We also demonstrated that citrate functionalized NPs induce multiple photoluminescence (PL) processes. We further investigated the photocatalytic activity of citrate functionalized NPs using Methylene Blue (MB) as a model organic pollutant. The effect of doping metal ions (Cu^{2+} and Fe^{3+}) on the photoluminescence and catalytic activity of the NPs has also been investigated. In order to fabricate prototypes for potential applications, we have immobilized citrate functionalized Mn_2O_3 microspheres on a stainless steel mesh and confirmed the filtering activity of the mesh to suspended particulates and catalytic degradation of a model contaminant in the presence of light.

2. Materials and methods

2.1. Synthesis of materials

Manganese acetate dihydrate, sodium citrate, sodium hydroxide, copper chloride dihydrate, ferric chloride, methylene blue and Nafion were purchased from Sigma Aldrich. Potassium bromide and ethylene glycol were obtained from Merck. The stainless steel mesh was purchased from Shangyu metal mesh company, China. All other chemicals employed were of analytical grade and used without further purification. In a typical synthesis of Mn_2O_3 microspheres, 0.03 mol of manganese acetate dihydrate and 0.27 mol of urea were added into 30 ml ethylene glycol to form the solution.[38] The resultant mixture was continuously stirred for 2 hours and then transferred into a 30 mL Teflon-lined stainless-steel autoclave. The Teflon-lined autoclave was put into an oven at 180 °C for 24 hours. The system was then cooled to ambient temperature naturally. The final product was collected and washed with distilled water and absolute alcohol at least five times. Then as-prepared samples were further annealed at 500 °C for 10 hours in air.[39] The synthesis of metal ion doped manganese oxides microspheres designated as Cu–Mn_2O_3 and Fe–Mn_2O_3 was carried out by addition of 0.003 M copper chloride dihydrate and 0.003 M ferric chloride, respectively, under similar reaction conditions.

For the citrate functionalization of the Mn_2O_3 microspheres (C–Mn_2O_3 NPs), 0.5 M sodium citrate was prepared in Milli-Q water. Then 10 mg of Mn_2O_3 microspheres were added, followed by extensive mixing for 16 hours in a cyclo mixer. Finally, the non-functionalized bigger particles were filtered out and the resulting filtrate solution was used. In the same way, citrate functionalized doped Mn_2O_3 NPs (C–Fe–Mn_2O_3 and C–Cu–Mn_2O_3) were synthesized. For the surface modification of the citrate functionalized NPs the pH of the solution was adjusted to 12 by addition of 1 M sodium hydroxide. The resulting solution was then finally heated at 60 °C for 12 hours. Finally, the solution became highly photoluminescent and the color of the solution turned into yellowish-brown. Generally, Mn^{3+} in an acid/neutral solution is unstable and has a tendency to disproportionate into Mn^{2+} and Mn^{4+}, whereas in an alkali medium it is stabilized by comproportionation of Mn^{4+} and Mn^{2+}.[40] The C–Fe–Mn_2O_3 and C–Cu–Mn_2O_3 samples can also become highly luminescent by the above-described treatment.

In order to prepare microspheres on a stainless steel mesh, initially the mesh was cleaned through bath sonication in acetone for 30 min and dried on a hot-plate at 60 °C. Then deposition of C–Mn_2O_3 on the mesh was done using a nebulizer followed by annealing at 400 °C for 10 hours, which has been used as a seeding layer for the synthesis of Mn_2O_3 microspheres. Then, 0.03 mol of manganese acetate dihydrate and 0.27 mol of urea were dissolved into 30 ml ethylene glycol. The resultant mixture was continuously stirred for 2 h and then transferred into a 30 mL Teflon-lined stainless-steel autoclave containing the mesh. The Teflon-lined autoclave was put into an oven at 180 °C for 24 h. The system was then cooled to ambient temperature. Then the mesh was washed thoroughly with water to remove excess unreacted reagents. The as-synthesized Mn_2O_3 microspheres

on the mesh were further annealed at 500 °C for 10 h in air. The Cu–Mn_2O_3 and Fe–Mn_2O_3 microspheres on the mesh were synthesized by following the above-mentioned conditions with the addition of 0.003 M copper chloride dihydrate and ferric chloride, respectively. Then the functionalization of the microspheres by citrate was performed accordingly.

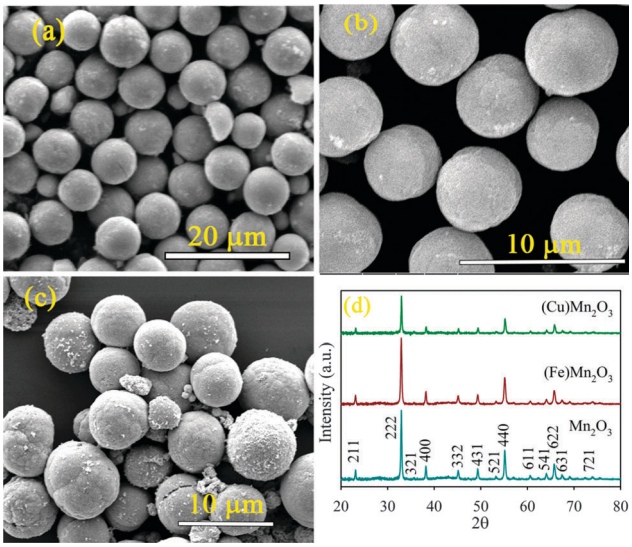

Fig. 1 FESEM images of (a) Mn_2O_3, (b) Fe doped Mn_2O_3 and (c) Cu doped Mn_2O_3 microsphere samples. (d) XRD pattern of Mn_2O_3, Fe doped Mn_2O_3 and Cu doped Mn_2O_3.

2.2. Characterization

Field emission scanning electron microscopy (FESEM, QUANTA FEG 250) investigations were performed by applying a diluted drop of NPs on a silicon wafer. Transmission electron microscopy (TEM) grids were prepared by applying a diluted drop of the citrate functionalized NP samples to carbon-coated copper grids. The particle sizes were determined from micrographs recorded at a magnification of 100000X using an FEI (Technai S-Twin, operating at 200 kV) instrument. X-ray diffraction (XRD) patterns of the samples were obtained by employing a scanning rate of 0.02° S^{-1} in the 2θ range from 20° to 80° using a PANalytical XPERTPRO diffractometer equipped with Cu Kα radiation (at 40 mA and 40 kV). FTIR spectra of the as prepared samples were recorded on a JASCO FTIR-6300 spectrometer, using a CaF_2 window. Raman scattering experiments were performed in back-scattering geometry using a micro-Raman setup consisting of a spectrometer (LabRAM HR, Jobin Yvon) and a peltier-cooled charge-coupled device (CCD) detector. An air cooled argon ion laser with a wavelength of 488 nm was used as the excitation light source. Raman spectra of all the samples have been recorded at room temperature in the frequency range 50–4000 cm^{-1}. X-ray photoelectron spectroscopy (XPS) measurements were performed using a Kratos Axis Ultra DLD spectrometer equipped with a monochromatic Al K_α X-ray source ($h\nu$ = 1486.6 eV) operated at 150 W, a multichannel plate, and a delay line detector under a vacuum of 1.3×10^{-19} Torr. More details can be found elsewhere.[41] For steady state and time resolved optical study we have followed the methodology as described in our earlier work.[42]

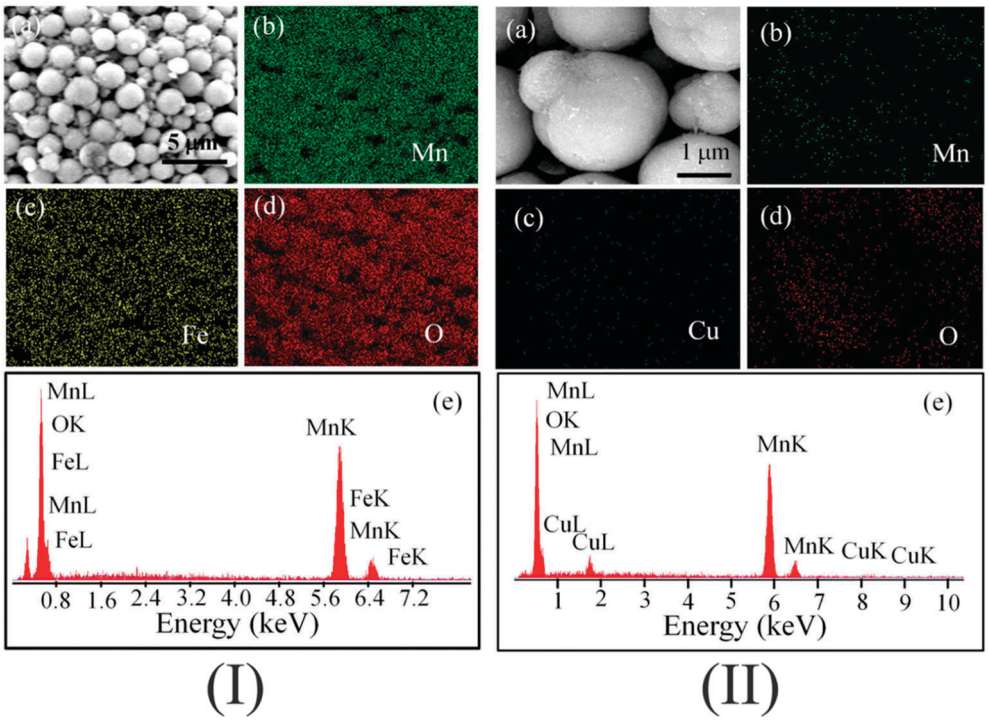

Fig. 2 (I) (a) SEM image, (b) Mn, (c) Fe, and (d) O elemental mapping images of Fe doped Mn_2O_3 microspheres. (e) EDAX spectrum of Fe doped Mn_2O_3 microspheres. (II) (a) SEM image, (b) Mn, (c) Cu, and (d) O elemental mapping images of Cu doped Mn_2O_3 microspheres. (e) EDAX spectrum of Cu doped Mn_2O_3 microsphere.

For electrochemical measurements cyclic voltammetry (CV) was carried out in an electrochemical cell using 0.01 M KCl electrolyte. 2 mg of Mn_2O_3 sphere and 6 mg of C–Mn_2O_3 were dissolved in 50 μl of ethanol containing 5 wt% Nafion as a binder. Then 10 μl of sample solution were deposited on glassy carbon (working electrode). CV was carried out using CH Instruments and swept at 50 mV S^{-1} between 0 and 3 V applied *versus* an Ag/AgCl reference electrode.

For photocatalysis studies, citrate functionalized NPs were taken in deionized water (DI) and methylene blue in DI was used as the test contaminant. An 8 W UV source was used as an irradiation source in this study. The mixture of photocatalyst and contaminant was irradiated with UV irradiation and absorbance data were collected continuously by using a setup reported earlier.[43] The percentage degradation (%DE) of MB was determined using:

$$\%\mathrm{DE} = \frac{I_0 - I}{I_0} \times 100 \quad (1)$$

where I_0 is the initial absorption intensity of MB at λ_{max} = 660 nm and I is the absorption intensity after UV irradiation.

3. Results and discussion

Fig. 1a–c show the morphology of the as-synthesized Mn_2O_3 microspheres without and with Fe^{+3}/Cu^{+2} doping as revealed from FESEM. The average sizes of the native, Fe (Fe–Mn_2O_3) and Cu (Cu–Mn_2O_3) doped Mn_2O_3 microspheres are found to be 6–8 μm, 4–6 μm and 5–7 μm, respectively. Fig. 1d shows XRD patterns of native Mn_2O_3, Fe–Mn_2O_3 and Cu–Mn_2O_3, respectively. XRD patterns of Fe–Mn_2O_3 and Cu–Mn_2O_3 are similar to that of native bare Mn_2O_3 and consistent with the diffraction pattern of pristine bulk Mn_2O_3 reported in the literature.[38] During doping of bulk Mn_2O_3, the Cu^{2+} ion can easily replace Mn^{3+} in the crystal lattice due to the

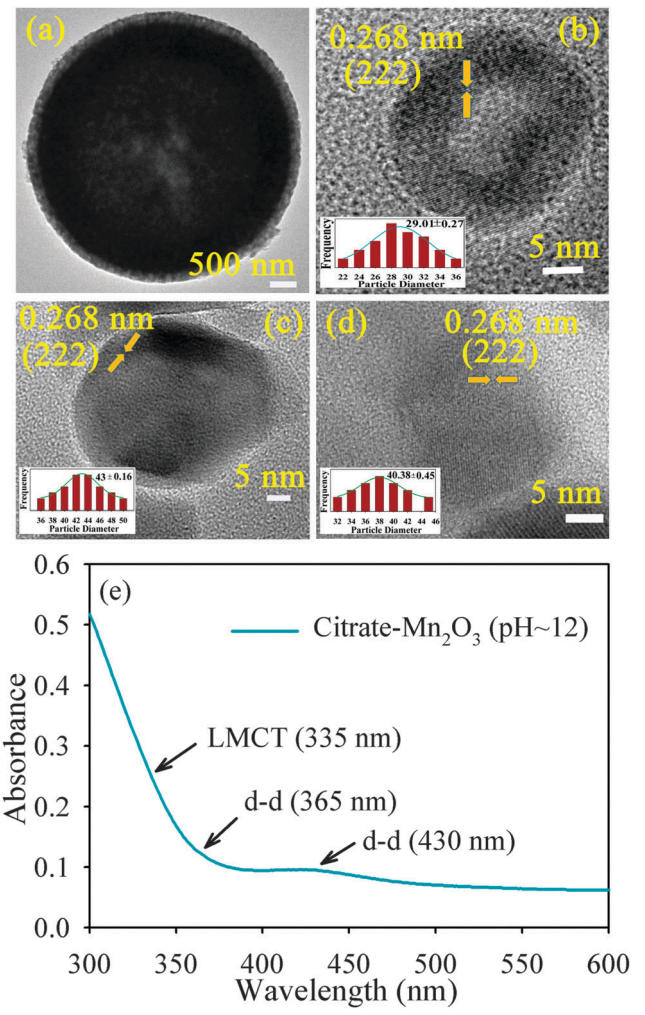

Fig. 3 TEM image of Mn_2O_3 microspheres (a), C–Mn_2O_3 (b), Fe doped C–Mn_2O_3 (c) and Cu doped C–Mn_2O_3 (d) NPs (inset shows size distribution of NPs). (e) UV-vis absorption spectrum of C–Mn_2O_3 NPs (at pH ~12 and 70 °C for 12 h).

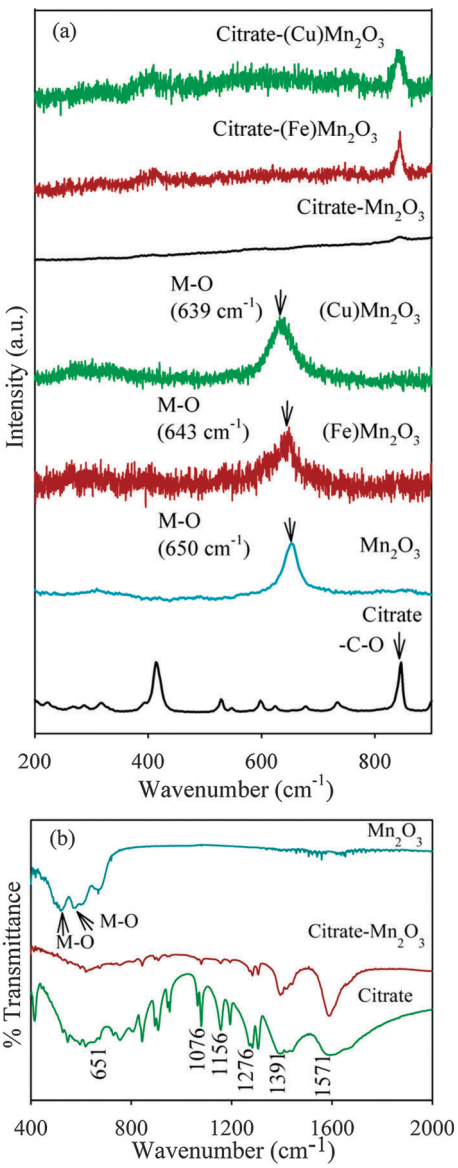

Fig. 4 (a) Raman spectra of the citrate, Mn_2O_3, Fe doped Mn_2O_3, Cu doped Mn_2O_3, C–Mn_2O_3, Fe doped C–Mn_2O_3 and Cu doped C–Mn_2O_3. (b) FTIR spectra of citrate, C–Mn_2O_3 and Mn_2O_3 respectively.

smaller radius of the Cu^{2+} ion (0.057 nm) compared to that of Mn^{3+} (0.066). Similarly the substitution of the Mn^{3+} ion by Fe^{3+} occurs due to the smaller radius of the Fe^{3+} ion (0.063).[44,45]

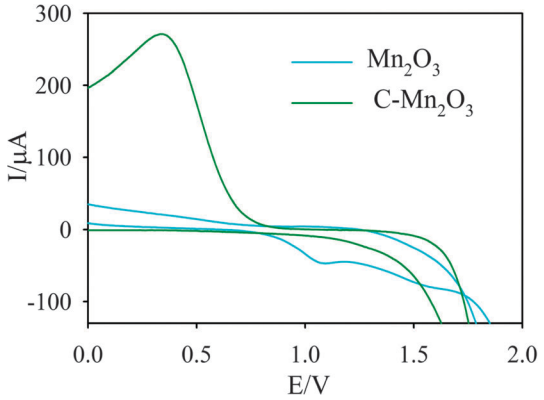

Fig. 5 Cyclic voltammogram of bare Mn_2O_3 (cyan line) and Mn_2O_3 after functionalization with citrate (green line) recorded at a scan rate 50 mV S^{-1} in the range of 0 to 3 V using Ag/AgCl as a reference electrode.

In order to confirm the uniform distribution of Fe and Cu atoms in the Fe–Mn_2O_3 and Cu–Mn_2O_3 microspheres we have performed elemental EDAX mapping as shown in Fig. 2. From the EDAX measurement, it is observed that 2.5 wt% of Fe is doped into the Mn_2O_3 crystal and 1.96 wt% of Cu is doped into the Mn_2O_3 crystal lattice. TEM was used in order to investigate the microscopic structure of as synthesized Mn_2O_3 microspheres (Fig. 3a). Upon interaction with citrate ligands the Mn_2O_3 microspheres become water soluble and smaller in size as evident from the HRTEM image (Fig. 3b). The citrate functionalized Mn_2O_3 nanoparticles (C–Mn_2O_3 NPs) are found to have a size distribution with an average diameter of 29.01 ± 0.27 nm (inset of Fig. 3b). The HRTEM images of C–Mn_2O_3 NPs also show the high crystallinity of the NPs. The inter-planar distance between the fringes is found to be about 0.268 nm consistent with (222) planes of bulk Mn_2O_3.[46] The citrate functionalized Fe doped Mn_2O_3 and Cu doped Mn_2O_3 NPs are found to have an average size of 43 ± 0.16 and 40.38 ± 0.45 nm respectively. HRTEM images also indicate the highly crystalline nature of citrate functionalized Fe doped Mn_2O_3 and Cu doped Mn_2O_3 NPs.

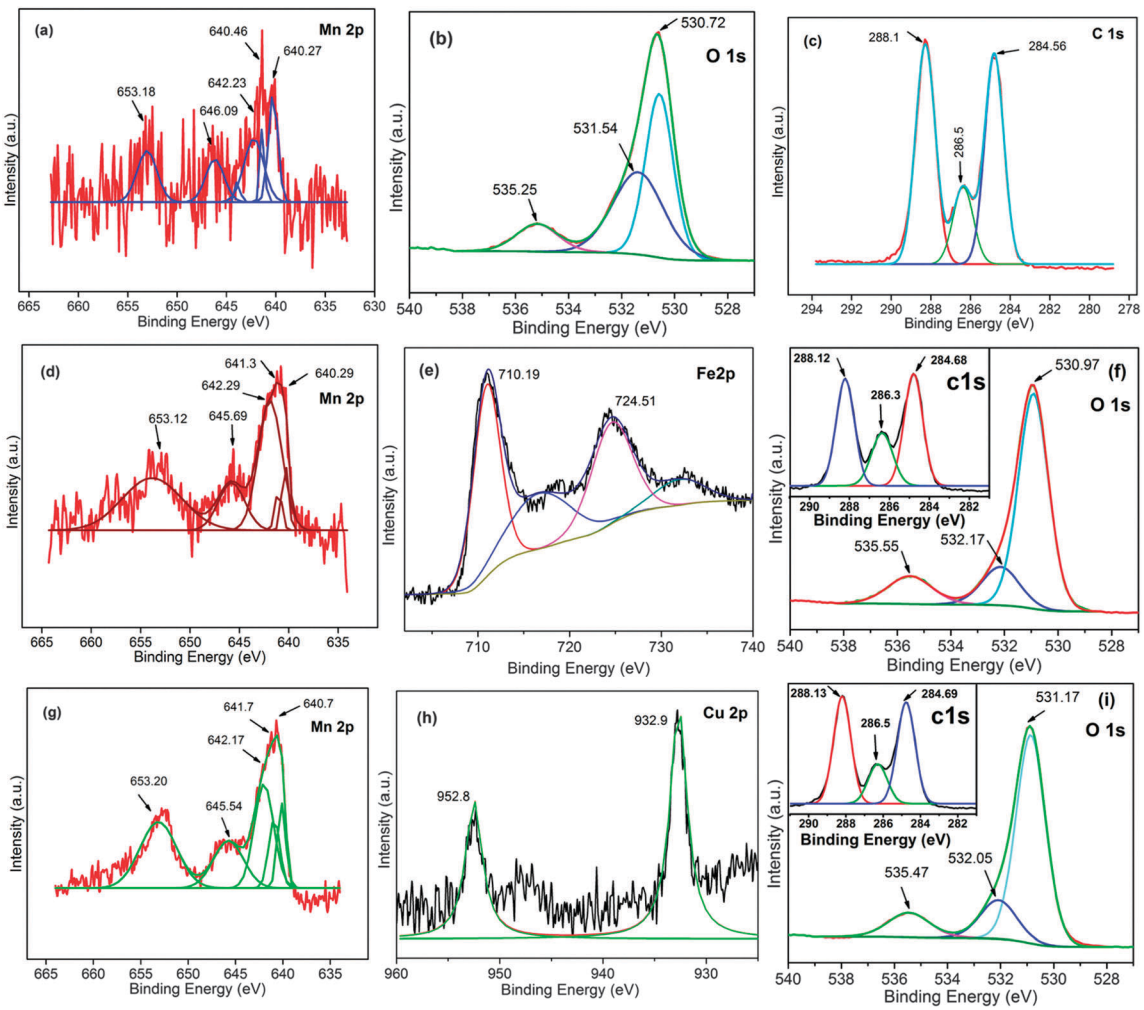

Fig. 6 XPS spectra of C–Mn_2O_3 NPs (a) Mn 2p, (b) O 1s, and (c) C 1s. XPS spectra of Fe doped C–Mn_2O_3 NPs (d) Mn 2p, (e) Fe2p, and (f) O 1s (inset shows C 1s). XPS spectra of Cu doped C–Mn_2O_3 NPs (g) Mn 2p, (h) Cu2p, and (i) O 1s (inset shows C 1s).

The effect of citrate functionalization of the NPs is evident in the UV-Vis absorbance spectra of the NPs at room temperature. While the citrate ligand and native Mn_2O_3 do not show any characteristic peak in the wavelength range of 300–600 nm, functionalized NPs show several absorption peaks (at 335, 365 and 430 nm) in the wavelength window (as shown in Fig. 3e).[3,47] The observed peak at 335 nm may be assigned to high energy ligand to metal charge transfer (LMCT) processes involving citrate–Mn^{3+} interactions. The other peaks at 365 and 430 nm correspond to the d–d transitions of Mn^{3+} in Mn_2O_3 NPs since Mn^{3+} (d^4) forms a high spin complex. The ground state term of Mn^{3+} (d^4) is 5E in Mn_2O_3 from the high spin complex which undergoes a Jahn–Teller distortion due to functionalization with citrate. This leads to band transitions of $5B_1$–$5E$, $5B_1$–$5B_2$ and $5B_1$–$5A_1$.[48,49] Fig. 4a shows Raman spectra of the ligand, bare Mn_2O_3 and C–Mn_2O_3 revealing the structural modification of Mn_2O_3 NPs upon functionalization with the citrate ligand. The main characteristic peak observed at 650 cm^{-1} of Mn_2O_3 NPs corresponds to M–O stretching vibrations,[50] and C–O stretching vibration of the citrate ligand located at 843 cm^{-1} are perturbed upon functionalization with citrate. This indicates the covalent binding of the citrate ligand with the NP surface. Similar changes are observed for Fe–Mn_2O_3 and Cu–Mn_2O_3 after citrate functionalization as shown in Fig. 4a. A strong electronic coupling of the ligand with Mn_2O_3 NPs is also evident from FTIR spectra as shown in Fig. 4b. Bare Mn_2O_3 shows two characteristic bands at 576 and 521 cm^{-1} corresponding to M–O stretching vibrations of Mn_2O_3 NPs.[51] After functionalization with citrate ligands, the bands are distinctly diminished indicating strong interaction between Mn_2O_3 NPs and the citrate ligand. It is also observed that two sharp bands at 1156 and 1076 cm^{-1} responsible for the C–O stretching modes of citrate[52] are broadened in C–Mn_2O_3 NPs. This observation is consistent with the fact that the carboxylate functional group in the citrate makes covalent bonding with the NP surface.

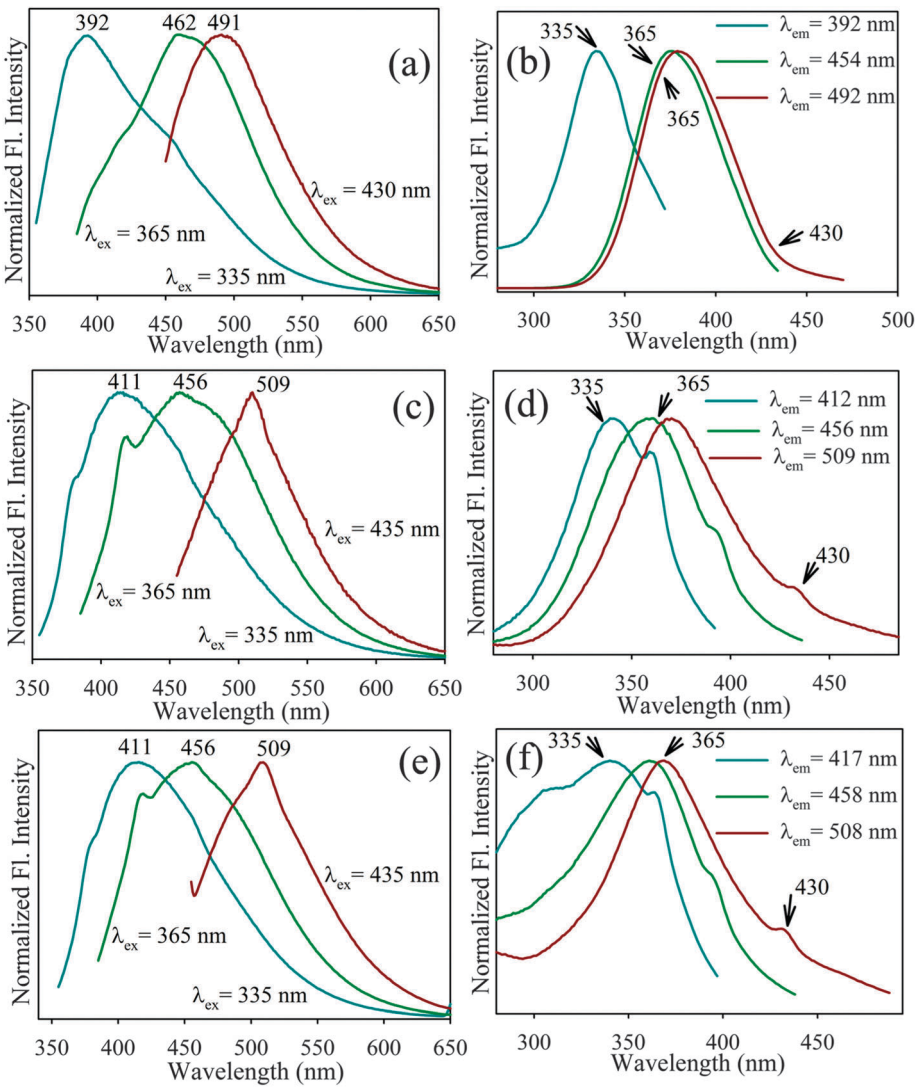

Fig. 7 (a), (c) and (e) are normalized steady-steady PL spectra collected from C–Mn_2O_3, Fe doped C–Mn_2O_3 and Cu doped C–Mn_2O_3 NPs respectively at three different excitation wavelengths at pH ~ 12. Figure (b), (d) and (f) are the excitation spectra of C–Mn_2O_3, Fe doped C–Mn_2O_3 and Cu doped C–Mn_2O_3 NPs, respectively, at different PL maxima.

A clear change in the redox property of bare Mn_2O_3 upon citrate functionalization is evident from CV measurements as shown in Fig. 5. It is known that for bare Mn_2O_3, the first reduction process at $\sim$1.1 V corresponds to the reduction of Mn^{3+} to Mn^{2+}.[53] As evident from Fig. 5, the reduction peak at 1.06 V for bare Mn_2O_3 is significantly perturbed upon functionalization and a new peak at $\sim$0.35 V appears for Mn_2O_3 NPs. This peak can be attributed to the oxidation of Mn^{+3}/Mn^{+4} species.[54] This implies that after functionalization in Mn_2O_3 the charge state of Mn^{3+} disproportionates and is generate dominantly by the +4 charge state. It has to be noted that the formation of the +2 state as a result of disproportionation is not clear from these CV studies, however, evident in the XPS spectrum. Fig. 6 shows XPS spectra of Mn_2O_3, Fe–Mn_2O_3 and Cu–Mn_2O_3 after citrate functionalization. As reported in the earlier studies Mn_2O_3 shows two Mn 2p peaks at 642.40 and 654.13 eV, which are attributed to Mn $2p_{3/2}$ and Mn $2p_{1/2}$, respectively.[55] A spin energy gap of 11.73 eV is reported to be a significant signature of Mn^{3+} in Mn_2O_3.[56] As shown in Fig. 6a the XPS spectrum (Mn 2p) for C–Mn_2O_3 can be deconvoluted into four peaks at 640.27, 640.46, 642.23 and 653.18 eV. While 640.27 eV can be attributed to Mn^{2+}, 640.46 and 642.23 eV correspond to Mn^{3+} and Mn^{4+} respectively.[57,58] The Mn $2p_{1/2}$ at 653.18 eV indicates a +3 oxidation state of Mn assuming the peak at 646.09 eV to be a shake-up satellite.[32] The deconvoluted O 1s line spectra are composed of three peaks. The O 1s line at 530.72 eV corresponds to the surface hydroxyl groups and the peaks at 531.54 and 535.25 eV indicate the presence of adsorbed water molecules.[59] Again, the deconvoluted C 1s line spectra were recorded with three peaks to analyze the interactions between the citrate ligand and NPs. The C 1s peak at 284.56, 286.50 and 288.10 eV can be assigned to carbon present in citrate in the form of C–C, C–OH and COO, respectively.[60] Therefore, functionalization with citrate suppresses the +3 oxidation state of Mn and generates +4 and +2 states *via* a disproportionation mechanism.[61] As shown in Fig. 6, similar changes in the oxidation state of Mn for Fe–Mn_2O_3 and Cu–Mn_2O_3 NPs after citrate functionalization are evident. The XPS spectrum of Fe doped Mn_2O_3 shows two Fe 2p peaks at 710.19 and 724.51 eV which can be attributed to Fe $2p_{3/2}$ and Fe $2p_{1/2}$ respectively.[62,63] This indicates incorporation of Fe into the lattice of Mn_2O_3.The XPS spectrum of Cu doped Mn_2O_3 illustrates two Cu 2p peaks at 932.9 and 952.8 eV, which can be attributed to Cu $2p_{3/2}$ and Cu $2p_{1/2}$, respectively.[38,64,65] The observation confirms the incorporation of Cu into the lattice of Mn_2O_3.

Fig. 7a shows normalized fluorescence spectra of C–Mn_2O_3 NPs at room temperature at pH 12. C–Mn_2O_3 NPs show multiple photoluminescence (PL maxima at 392, 462 and 491 nm) upon excitation at different wavelengths (335, 365 and 430 nm, respectively). Fig. 7b shows excitation spectra of C–Mn_2O_3 NPs with different emission wavelengths. The ligand field theory can be useful in order to understand the multiple PL of the C–Mn_2O_3 NPs.[66,67] Multiple PL of the C–Mn_2O_3 NPs arise mainly due to the LMCT (citrate–Mn^{3+}) excited states and the ligand field excited states of the metal (Mn^{3+}) d-orbitals. Thus the PL peak at 392 nm arises due to LMCT from HOMO (highest occupied molecular orbital, centered in the ligand) to LUMO (lowest unoccupied molecular orbital, centered in the metal centre). On the other hand, PL peaks at 462 and 492 nm arise due to d–d transition of the Mn^{3+} ion, in the presence of the citrate ligand. Similarly, multiple PL (maxima at 411, 456 and 509 nm) arises in C–Fe–Mn_2O_3 NPs and C–Cu–Mn_2O_3 NPs upon excitation at different wavelengths (335, 365 and 435 nm, see Fig. 7c and e). Fig. 7d and f shows excitation spectra of C–Fe–Mn_2O_3 NPs and C–Cu–Mn_2O_3 NPs detected at different PL maxima. It is observed that unfunctionalized Mn_2O_3, Fe–Mn_2O_3 and Cu–Mn_2O_3 have no such PL properties due to absence of LMCT and the J–T phenomenon. The multiple PL of the citrate functionalized NPs is further recorded under a fluorescence microscope, see Fig. 8. Fig. 8a–c shows bright field images and two fluorescence images of C–Mn_2O_3 NPs (excitation at 365 and 436 nm) respectively. C–Mn_2O_3 NPs upon 365 nm

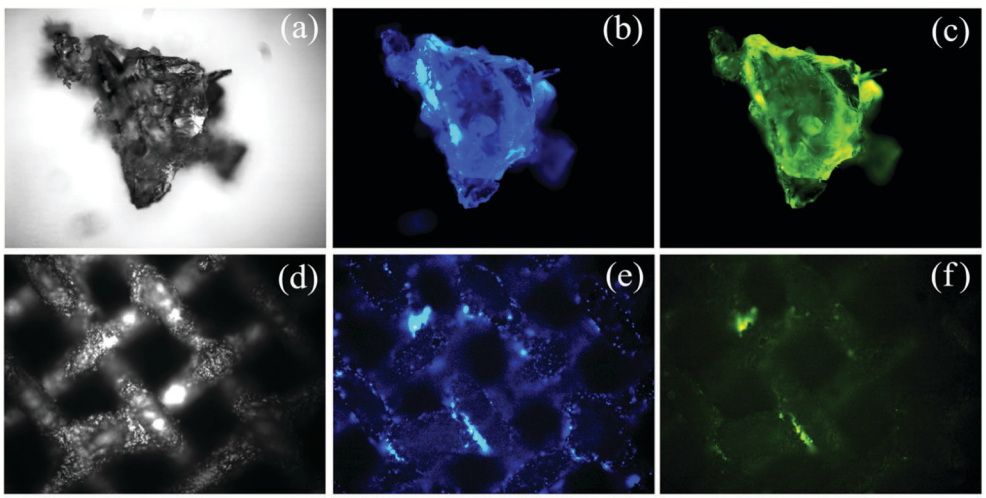

Fig. 8 Fluorescence microscopic images of the C–Mn_2O_3 NPs and mesh-C–Mn_2O_3 under white light (a and d) and light of two different wavelengths 365 nm (b and e) and 436 nm (c and f), respectively.

excitation show cyan emission and 436 nm excitation show green emission. Fig. 8d–f shows similar PL of functionalized Mn_2O_3 microspheres on the stainless steel mesh.

In order to investigate a detailed mechanistic insight into the origin of the multiple PL of the functionalized NPs, we have performed picosecond-resolved fluorescence studies. From Fig. 9, the fluorescence decay of the C–Mn_2O_3, C–Fe–Mn_2O_3 and C–Cu–Mn_2O_3 NPs was determined at different PL maxima of 456 and 507 nm using lasers as an excitation source at 375 and 445 nm, respectively. The lifetime values for 456 and 507 nm emission (upon excitation by 375 and 445 nm laser sources) decays are shown in Table 1. From this table it is shown that the average lifetimes of C–Mn_2O_3 are 2.01 and 1.95 ns when the PL is measured at 456 and 507 nm, respectively, upon 375 nm laser excitation, while it is 0.59 ns when PL is measured at 507 nm upon 445 nm laser excitation. The lifetime data clearly suggest that the Jahn–Teller distortion leads to PL maxima at 456 and 507 nm upon excitation at 375 and 445 nm, respectively. Here it is observed that after doping the J–T distorted d–d transition leads to PL maxima at 456 and 507 nm. The average lifetimes of C–Fe–Mn_2O_3 are 0.76 and 0.94 ns, respectively, upon 375 laser excitation, while it is 0.34 ns when PL is measured at 507 nm upon 445 nm laser excitation. The decrease in the average lifetime after iron doping may be attributed to the faster electron transfer from C–Mn_2O_3 to Fe^{+3}. The average lifetimes of C–Cu–Mn_2O_3 are 0.74 and 0.91 ns upon 375 nm laser excitation while it is 0.33 ns when PL is measured at 507 nm upon 445 nm laser excitation. The decrease in average lifetimes indicates an additional nonradiative time scale in the excited state which can alter the fluorescence lifetimes. The apparent rate constant (k_{nr}) is determined for the nonradiative processes by comparing the lifetimes of citrate functionalized Mn_2O_3 NPs in the absence (τ_0) and presence (τ) of the doping metal ion, using the equation.

$$k_{nr} = \frac{1}{\langle\tau\rangle} - \frac{1}{\langle\tau_0\rangle} \quad (2)$$

The apparent rate constant values for Fe doped C–Mn_2O_3 and Cu doped C–Mn_2O_3 are shown in Table 1 which indicates the excited state electron transfer from C–Mn_2O_3 to Fe and Cu.

It has been reported that adsorption plays an important role in the removal of pollutants.[68–71] However, in our case the as prepared microsphere has insignificant ability for methylene blue adsorption (data not shown). During the photocatalytic reaction, MB forms a well-known colorless product leucomethylene blue (LMB)[72,73] as shown in eqn (3).

$$2MB + 2e^- + H^+ = MB + LMB \quad (3)$$

In order to confirm the formation of leucomethylene blue, the degradation of methylene blue was performed in the presence of citrate capped Mn_2O_3 NPs under UV light irradiation and the absorption spectra were monitored at different time intervals. As shown in Fig. 10a, the methylene blue peak at 664 nm decreases with time whereas another peak at 246 nm corresponding to the leucomethylene blue formation increases during photocatalysis. As shown in Fig. 10b, no degradation of MB is observed in the absence of light. With our experimental time window,

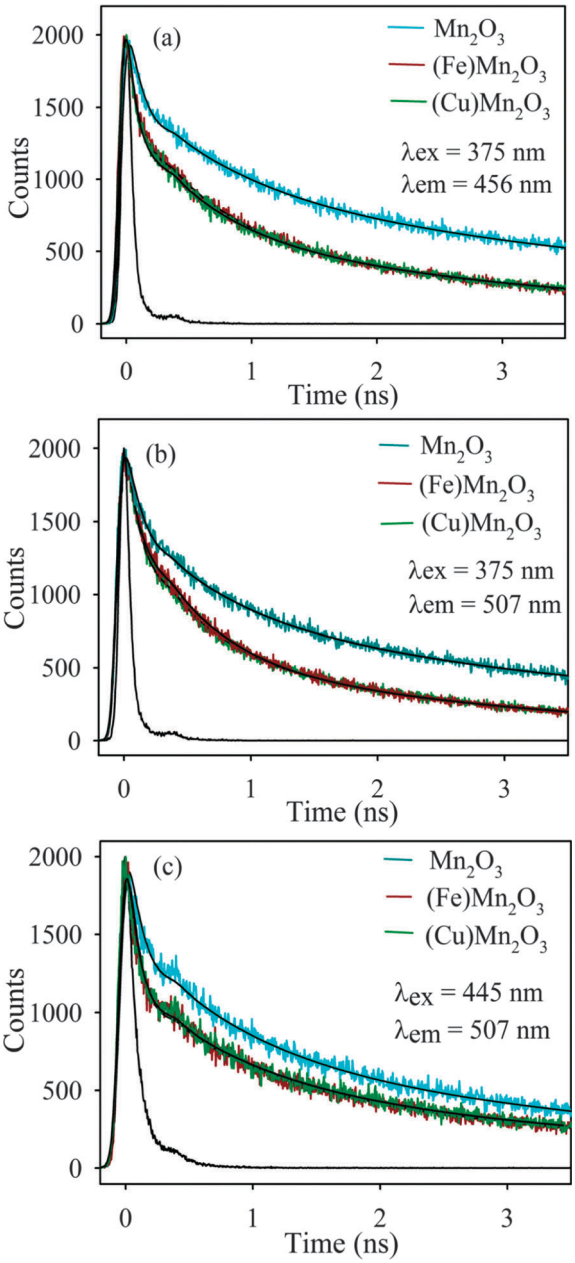

Fig. 9 (a) and (b) are the picosecond-resolved PL transients of C–Mn_2O_3 NPs, Fe doped C–Mn_2O_3 NPs and Cu doped C–Mn_2O_3 NPs measured at emission wavelengths 456 nm (I) and 507 nm (II) upon excitation at a wavelength of 375 nm. (c) Picosecond-resolved PL transients of C–Mn_2O_3 NPs, Fe doped C–Mn_2O_3 NPs and Cu doped C–Mn_2O_3 NPs measured at an emission wavelength of 507 nm upon excitation at wavelength of 445 nm.

MB shows <10% degradation under light illumination in the absence of NPs. Under UV light illumination, C–Mn_2O_3 NPs show a 50% MB degradation after 80 minutes. It is important to note that with our experimental conditions (pH 3), Mn^{3+} ions easily disproportionate into Mn^{2+} and Mn^{4+}. So there is a possibility of d–d transitions involving $Mn^{2+/4+}$ ions on the C–Mn_2O_3 NP surface. According to the selection rules of fundamental electronic spectroscopy, LMCT bands (involving the interaction between the highest occupied molecular orbital

Table 1 Lifetimes of picosecond time-resolved PL transients of C–Mn_2O_3, Fe doped C–Mn_2O_3 and Cu doped C–Mn_2O_3 NPs, detected at various PL maxima upon excitation at different wavelengths. The values in parentheses represent the relative weight percentages of the time components

System	λ_{ex} (nm)	λ_{em} (nm)	τ_1 (ns)	τ_2 (ns)	τ_3 (ns)	τ_{avg} (ns)	k_{nr} (10^{10} s^{-1})
C–Mn_2O_3	375	456	0.08(58)	1.5(23)	8.6(19)	2.01	
		507	0.14(58)	1.65(26)	9.04(14)	1.95	
	445	507	0.04(80)	0.85(10)	4.59(10)	0.59	
Fe doped C–Mn_2O_3	375	456	0.06(69)	1.1(22)	5.35(9)	0.76	8.14
		507	0.15(62)	1.17(10)	5.4(10)	0.94	5.51
	445	507	0.03(88)	0.99(7)	5.26(5)	0.34	12.46
Cu doped C–Mn_2O_3	375	456	0.06(71)	1.13(20)	5.54(9)	0.74	8.53
		507	0.14(65)	1.2(26)	5.53(9)	0.91	5.86
	445	507	0.11(88)	0.9(6)	4.63(6)	0.33	13.35

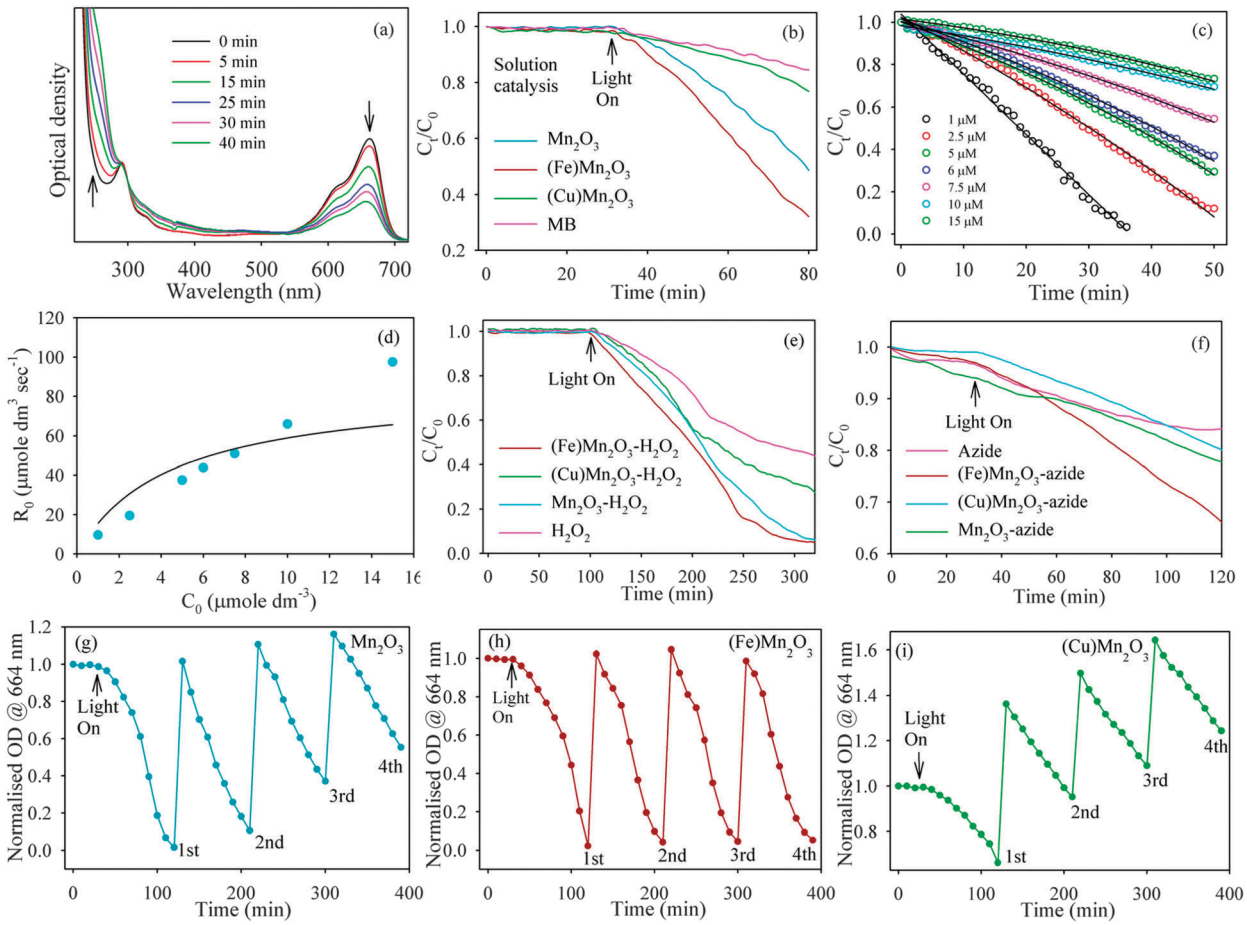

Fig. 10 Photocatalytic degradation of MB in the presence of (a) C–Mn_2O_3 (b) C–Mn_2O_3, Fe doped C–Mn_2O_3 and Cu doped C–Mn_2O_3 NPs in solution under UV light illumination. (c) C_t/C_0 *versus* time with various concentrations of methylene blue. (d) Langmuir–Hinshelwood plot (L–H) for photocatalytic degradation of methylene blue using citrate functionalized Mn_2O_3 nanoparticles (solid line is the model fitting and solid circles are experimental data). (e) Photocatalytic degradation of MB in the presence of hydrogen peroxide under UV light illumination. (f) Photocatalytic degradation of MB in the presence of sodium azide under UV light illumination. The recyclability study of C–Mn_2O_3 (g) Fe doped C–Mn_2O_3 (h) and Cu doped C–Mn_2O_3 (i) NPs under UV light illumination.

of citrate and the lowest unoccupied molecular orbital $Mn^{2+/4+}$) are mainly responsible for photocatalytic degradation of the model pollutant, MB. After doping with Fe, the photocatalytic activity of C–Fe–Mn_2O_3 NPs shows 65% MB degradation under UV light illumination. However, in C–Cu–Mn_2O_3 NPs the photocatalytic activity decreases to 20%. As compared to other catalysts reported in the literature, the photocatalytic activity of citrate functionalized Fe doped Mn_2O_3 NPs used in this work shows better catalytic activity.[20,21,31,74–76] In order to find out the effect of the surface on photocatalysis, the Langmuir–Hinshelwood (L–H) kinetics has been studied using different concentrations of MB. From Fig. 10c and d it is observed that

the surface does not play any role in photocatalysis since a huge deviation of the model from experimental data is evident.

In order to investigate the catalytic pathway, we further studied the photocatalytic activity of citrate functionalized NPs in the presence of a radical initiator (H_2O_2) and radical quencher (sodium azide) separately. The photocatalytic activity of citrate functionalized NPs increases in the presence of H_2O_2 indicating a role of reactive oxygen species (ROS) in the degradation of MB.[32] Actually, in the presence of H_2O_2 and under UV light illumination, the generation of $^{\bullet}OH$ increases the enhanced photocatalytic activity. We further studied the effect of sodium azide (a ROS quencher) on the degradation of MB by citrate functionalized NPs under UV light illumination. Fig. 10f clearly shows that in the presence of sodium azide the degradation rate of MB becomes slower. This indirectly confirms that the reaction proceeds *via* a ROS mechanism. The increase in the photocatalytic activity of C–Fe–Mn_2O_3 NPs compared to C–Mn_2O_3 NPs may be due to the excited state electron transfer from Mn_2O_3 to Fe^{3+}. This excited state electron transfer may facilitate the charge separation. The regeneration of Fe^{3+} takes places *via* ROS generation in an aqueous medium that eventually enhances the photocatalytic activity of Fe–C–Mn_2O_3 NPs.[77,78] However, in the case of C–Cu–Mn_2O_3 an excited electron transfer from Mn_2O_3 to Cu^{2+} takes place which is evident from the TCSPC data. The regeneration of Cu^{2+} may take place efficiently through the ground state recovery of C–Mn_2O_3 and not *via* a ROS generation. To examine the stability of citrate functionalized nanoparticles, we examined the photocatalytic degradation of MB up to four cycles under UV light illumination at room temperature. The recyclability of C–Mn_2O_3, C–Fe–Mn_2O_3 and C–Cu–Mn_2O_3 NPs is shown in Fig. 10g–i. These data suggest that C–Fe–Mn_2O_3 NPs show good recyclability up to the fourth cycle, whereas the C–Mn_2O_3 and C–Cu–Mn_2O_3 degradation efficiency decreases with each cycle.

In order to explore possible applications of citrate functionalized NPs for waste water treatment a stainless steel mesh has been used as a template. Fig. 11a and b show pure Mn_2O_3 microspheres on the stainless steel mesh at low and high magnification, respectively. While the low magnification FESEM image of the mesh confirms attachment of Mn_2O_3 microspheres, the high magnification image shows the uniform size distribution of the microspheres ranging from 2.5–3.5 μm. Upon doping with Fe^{3+} and Cu^{2+} the average size distributions of the synthesized microsphere are 3.5–4.5 μm and 1.5–2 μm, respectively. We have successfully functionalized the microspheres in the mesh with the citrate ligand. Here, the photocatalytic activity of C–Mn_2O_3, C–Fe–Mn_2O_3 and C–Cu–Mn_2O_3 has been studied on the mesh using MB as a model contaminant under solar light illumination. The pH of the solution is maintained at 6. The area of the mesh used in the photocatalytic study was 2 cm × 1.5 cm. From Fig. 11e it is evident that in the absence of light the citrate functionalized microspheres show no photocatalytic activity. However, under solar light illumination C–Mn_2O_3 exhibits 25% degradation, while the photocatalytic activity of C–Fe–Mn_2O_3 on the mesh increases to 34%. In the case of copper doping the photocatalytic activity of the sensitized C–Cu–Mn_2O_3 on the mesh decreases down to 12%. Under the same experimental conditions, MB in the absence of functionalized Mn_2O_3 microspheres shows no such degradation (7%). To our understanding such type of system is promising for water

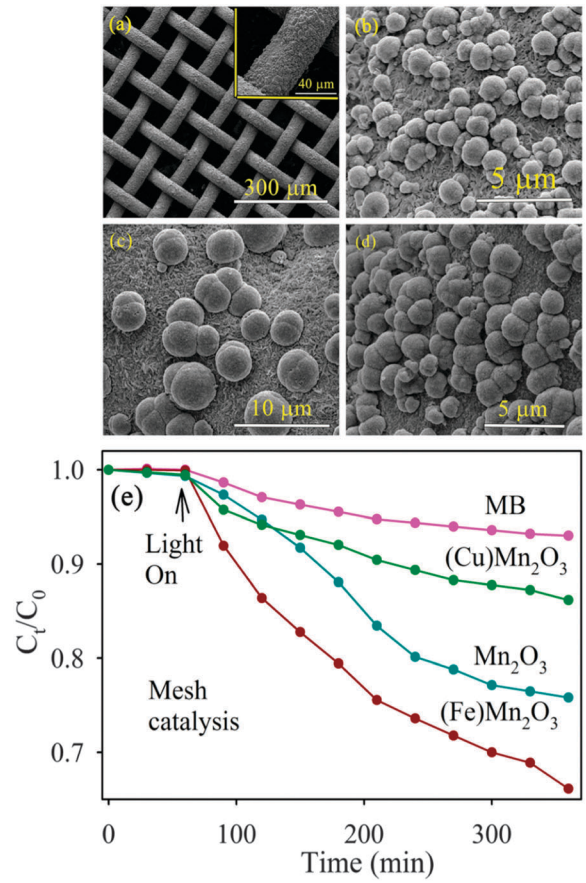

Fig. 11 (a) SEM images of Mn_2O_3 on the stainless steel mesh (inset shows high magnification). (b) SEM images of Mn_2O_3 on mesh in high magnification. (c) SEM images of Fe doped Mn_2O_3 on a mesh in high magnification. (d) SEM images of Cu doped Mn_2O_3 on a mesh in high magnification. (e) Photocatalytic degradation of MB by C–Mn_2O_3, Fe doped C–Mn_2O_3 and Cu doped C–Mn_2O_3 on the mesh under solar light illumination.

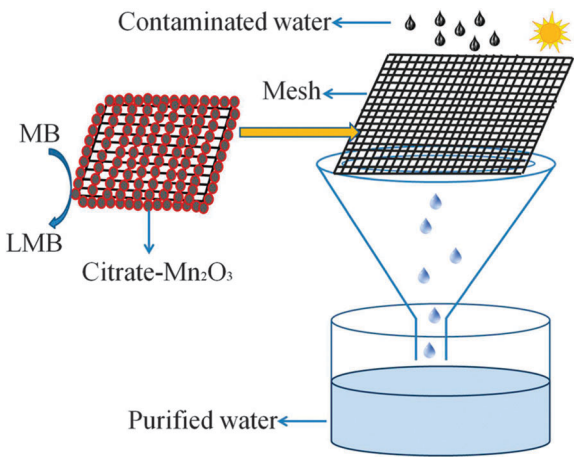

Scheme 1 Schematic representation of water purification by citrate functionalized Mn_2O_3 under solar light illumination.

purification both by physical (filtration) and chemical (photocatalysis) processes. Earlier Ochiai *et al.* showed that a TiO_2 enhanced Ti mesh filter is very much useful in water purification.[79] Li *et al.* showed that a Ti/TiO_2 mesh photoelectrode is an excellent system for photocatalytic degradation of humic acid in an aqueous solution.[80] In comparison with these earlier reports, our system is more cost effective if large scale water purification systems are concerned (Scheme 1).

4. Conclusions

In summary, we have successfully synthesized Mn_2O_3 microspheres *via* a hydrothermal route. The surface modification of the synthesized microspheres with citrate leads to new optical and functional properties. A detail spectroscopic investigation leads to the conclusion that J–T splitting of the Mn^{3+} ions and the LMCT bands are mainly responsible for the origin of such optical properties. The photocatalytic activity under solar light illumination of the citrate functionalized microspheres embedded on a mesh has also been studied using Methylene Blue as a model contaminant. Tuning of the photocatalytic activity of the microspheres upon doping with metal ions (Fe^{3+} and Cu^{2+}) has been demonstrated and correlated with intra-particle electron transfer. We have also realized a prototype for a larger scale water purification system using an ''active filter'', where the citrate functionalized Mn_2O_3 microspheres are attached on a stainless steel mesh. The system is supposed to filter suspended particulates and decontaminate water soluble pollutants in the presence of solar light.

Acknowledgements

P.K. thanks Council of Scientific and Industrial Research (CSIR, India) for fellowships. We thank the Department of Science and Technology (DST, India) for financial grants DST/TM/SERI/2k11/103 and SB/S1/PC-011/2013. We also thank DAE (India) for financial grant 2013/37P/73/BRNS. PL thanks the NTH-School ''Contacts in Nanosystems: Interactions, Control and Quantum Dynamics'', the Braunschweig International Graduate School of Metrology, and DFG-RTG 1953/1, Metrology for Complex Nanosystems. The authors would like to thank Dr Abhijit Saha, UGC-DAE Consortium for Scientific Research, Kolkata center, for his assistance in Raman experiments.

References

1 R. Hu, X.-B. Zhang, R.-M. Kong, X.-H. Zhao, J. Jiang and W. Tan, *J. Mater. Chem.*, 2011, **21**, 16323–16334.
2 Y.-P. Sun, K. Fu, Y. Lin and W. Huang, *Acc. Chem. Res.*, 2002, **35**, 1096–1104.
3 A. Giri, A. Makhal, B. Ghosh, A. K. Raychaudhuri and S. K. Pal, *Nanoscale*, 2010, **2**, 2704–2709.
4 P. Sahu and B. L. V. Prasad, *Langmuir*, 2014, **30**, 10143–10150.
5 G. Palui, F. Aldeek, W. Wang and H. Mattoussi, *Chem. Soc. Rev.*, 2015, **44**, 193–227.
6 M. A. H. Muhammed, F. Aldeek, G. Palui, L. Trapiella-Alfonso and H. Mattoussi, *ACS Nano*, 2012, **6**, 8950–8961.
7 C. S. S. R. Kumar and F. Mohammad, *Adv. Drug Delivery Rev.*, 2011, **63**, 789–808.
8 V. Polshettiwar, R. Luque, A. Fihri, H. Zhu, M. Bouhrara and J.-M. Basset, *Chem. Rev.*, 2011, **111**, 3036–3075.
9 A. Ito, M. Shinkai, H. Honda and T. Kobayashi, *J. Biosci. Bioeng.*, 2005, **100**, 1–11.
10 R. Hao, R. Xing, Z. Xu, Y. Hou, S. Gao and S. Sun, *Adv. Mater.*, 2010, **22**, 2729–2742.
11 S. Dhar, P. Murawala, A. Shiras, V. Pokharkar and B. L. V. Prasad, *Nanoscale*, 2012, **4**, 563–567.
12 S. Sardar, S. Chaudhuri, P. Kar, S. Sarkar, P. Lemmens and S. K. Pal, *Phys. Chem. Chem. Phys.*, 2015, **17**, 166–177.
13 A. Giri, N. Goswami, C. Sasmal, N. Polley, D. Majumdar, S. Sarkar, S. N. Bandyopadhyay, A. Singha and S. K. Pal, *R. Soc. Chem. Adv.*, 2014, **4**, 5075–5079.
14 S. Ghosh, D. Ghosh, P. K. Bag, S. C. Bhattacharya and A. Saha, *Nanoscale*, 2011, **3**, 1139–1148.
15 S. Sardar, P. Kar and S. K. Pal, *J. Mat. NanoSci.*, 2014, **1**, 12–30.
16 K. T. Nguyen and Y. Zhao, *Nanoscale*, 2014, **6**, 6245–6266.
17 P. Li, C. Nan, Z. Wei, J. Lu, Q. Peng and Y. Li, *Chem. Mater.*, 2010, **22**, 4232–4236.
18 J. Xiao, X. M. Tian, C. Yang, P. Liu, N. Q. Luo, Y. Liang, H. B. Li, D. H. Chen, C. X. Wang, L. Li and G. W. Yang, *Sci. Rep.*, 2013, **3**, 3424.
19 G.-J. Lee, A. Manivel, V. Batalova, G. Mokrousov, S. Masten and J. Wu, *Ind. Eng. Chem. Res.*, 2013, **52**, 11904–11912.
20 R. Saravanan, V. K. Gupta, V. Narayanan and A. Stephen, *J. Taiwan Inst. Chem. Eng.*, 2014, **45**, 1910–1917.
21 X. Hong-Yu, H. Lin and Y. Qi-Zhi, *J. Inorg. Mater.*, 2011, **26**, 317–320.
22 T. Ahmad, K. V. Ramanujachary, S. E. Lofland and A. K. Ganguli, *J. Mater. Chem.*, 2004, **14**, 3406–3410.
23 F. Cheng, J. Zhao, W. Song, C. Li, H. Ma, J. Chen and P. Shen, *Inorg. Chem.*, 2006, **45**, 2038–2044.
24 Z. Chen, Z. Jiao, D. Pan, Z. Li, M. Wu, C.-H. Shek, C. M. L. Wu and J. K. L. Lai, *Chem. Rev.*, 2012, **112**, 3833–3855.
25 G. Salazar-Alvarez, J. Sort, S. Suriñach, M. D. Baró and J. Nogués, *J. Am. Chem. Soc.*, 2007, **129**, 9102–9108.
26 Z. W. Chen, Z. Jiao, M. H. Wu, C. H. Shek, C. M. L. Wu and J. K. L. Lai, *Prog. Mater. Sci.*, 2011, **56**, 901–1029.
27 C. Chen, G. Ding, D. Zhang, Z. Jiao, M. Wu, C.-H. Shek, C. M. L. Wu, J. K. L. Lai and Z. Chen, *Nanoscale*, 2012, **4**, 2590–2596.
28 L. Liu, X. Zhang, R. Wang and J. Liu, *Superlattices Microstruct.*, 2014, **72**, 219–229.
29 J. Cao, Y. Zhu, L. Shi, L. Zhu, K. Bao, S. Liu and Y. Qian, *Eur. J. Inorg. Chem.*, 2010, 1172–1176.
30 Y. Liu, Z. Chen, C.-H. Shek, C. M. L. Wu and J. K. L. Lai, *ACS Appl. Mater. Interfaces*, 2014, **6**, 9776–9784.
31 S. Chandra, P. Das, S. Bag, R. Bhar and P. Pramanik, *Mater. Sci. Eng., B*, 2012, **177**, 855–861.
32 A. Giri, N. Goswami, M. Pal, M. T. Zar Myint, S. Al-Harthi, A. Singha, B. Ghosh, J. Dutta and S. K. Pal, *J. Mater. Chem. C*, 2013, **1**, 1885–1895.

33 S. Patoux, L. Sannier, H. Lignier, Y. Reynier, C. Bourbon, S. Jouanneau, F. Le Cras and S. Martinet, *Electrochim. Acta*, 2008, **53**, 4137–4145.
34 L. Alonso and J. M. Palacios, *Energy Fuels*, 2002, **16**, 1550–1556.
35 R. Huang, Y. Liu, Z. Chen, D. Pan, Z. Li, M. Wu, C.-H. Shek, C. M. L. Wu and J. K. L. Lai, *ACS Appl. Mater. Interfaces*, 2015, **7**, 3949–3959.
36 N. Goswami, A. Baksi, A. Giri, P. L. Xavier, G. Basu, T. Pradeep and S. K. Pal, *Nanoscale*, 2014, **6**, 1848–1854.
37 M. Habeeb Muhammed, S. Ramesh, S. Sinha, S. Pal and T. Pradeep, *Nano Res.*, 2008, **1**, 333–340.
38 Q. Li, L. Yin, Z. Li, X. Wang, Y. Qi and J. Ma, *ACS Appl. Mater. Interfaces*, 2013, **5**, 10975–10984.
39 J. Li, S. Xiong, X. Li and Y. Qian, *J. Mater. Chem.*, 2012, **22**, 23254–23259.
40 T. Takashima, K. Hashimoto and R. Nakamura, *J. Am. Chem. Soc.*, 2011, **134**, 1519–1527.
41 A. Fihri, R. Sougrat, R. B. Rakhi, R. Rahal, D. Cha, M. N. Hedhili, M. Bouhrara, H. N. Alshareef and V. Polshettiwar, *ChemSusChem*, 2012, **5**, 1241–1248.
42 P. Kar, S. Sardar, E. Alarousu, J. Sun, Z. S. Seddigi, S. A. Ahmed, E. Y. Danish, O. F. Mohammed and S. K. Pal, *Chem. – Eur. J.*, 2014, **20**, 10475–10483.
43 S. S. Sinha, P. K. Verma, A. Makhal and S. K. Pal, *Rev. Sci. Instrum.*, 2009, **80**, 053109.
44 G. Z. Xing, J. B. Yi, J. G. Tao, T. Liu, L. M. Wong, Z. Zhang, G. P. Li, S. J. Wang, J. Ding, T. C. Sum, C. H. A. Huan and T. Wu, *Adv. Mater.*, 2008, **20**, 3521–3527.
45 D. Bravo and F. J. Lopez, *J. Phys.: Condens. Matter*, 1992, **4**, 10335.
46 G. Yang, W. Yan, J. Wang and H. Yang, *CrystEngComm*, 2014, **16**, 6907–6913.
47 J. Cao, Y. Zhu, K. Bao, L. Shi, S. Liu and Y. Qian, *J. Phys. Chem. C*, 2009, **113**, 17755–17760.
48 M. Matzapetakis, N. Karligiano, A. Bino, M. Dakanali, C. P. Raptopoulou, V. Tangoulis, A. Terzis, J. Giapintzakis and A. Salifoglou, *Inorg. Chem.*, 2000, **39**, 4044–4051.
49 F. Aguado, F. Rodriguez and P. Núñez, *Phys. Rev. B: Condens. Matter Mater. Phys.*, 2007, **76**, 094417.
50 C. Zhiwen, T. Shun, Z. Shuyuan, W. Jian, J. Sizhao, Z. Yuheng and S. Hisashi, *Jpn. J. Appl. Phys.*, 2000, **39**, 6293.
51 R. Manigandan, R. Suresh, K. Giribabu, L. Vijayalakshmi, A. Stephen and V. Narayanan, *AIP Conf. Proc.*, 2014, **1576**, 125–127.
52 A. K. Thottoli and A. K. A. Unni, *J. Nanostruct. Chem.*, 2013, **3**, 1–12.
53 F. M. Courtel, H. Duncan, Y. Abu-Lebdeh and I. J. Davidson, *J. Mater. Chem.*, 2011, **21**, 10206–10218.
54 T. Nathan, M. Cloke and S. R. S. Prabaharan, *J. Nanomater.*, 2008, **2008**, 948183.
55 P. Pal, A. K. Giri, S. Mahanty and A. B. Panda, *CrystEngComm*, 2014, **16**, 10560–10568.
56 J. W. Lee, A. S. Hall, J.-D. Kim and T. E. Mallouk, *Chem. Mater.*, 2012, **24**, 1158–1164.
57 F. Li, L. Zhang, D. G. Evans and X. Duan, *Colloids Surf., A*, 2004, **244**, 169–177.
58 H. Nesbitt and D. Banerjee, *Am. Mineral.*, 1998, **83**, 305–315.
59 F. Xiao and Y. Xu, *Int. J. Electrochem. Sci.*, 2012, **7**, 7440–7450.
60 A. S. Tselesh, *Thin Solid Films*, 2008, **516**, 6253–6260.
61 L. L. Zhang, T. Wei, W. Wang and X. S. Zhao, *Microporous Mesoporous Mater.*, 2009, **123**, 260–267.
62 Y. Dai and L. Yin, *J. Alloys Compd.*, 2013, **563**, 80–84.
63 T. Yamashita and P. Hayes, *Appl. Surf. Sci.*, 2008, **254**, 2441–2449.
64 S. Gao, S. Yang, J. Shu, S. Zhang, Z. Li and K. Jiang, *J. Phys. Chem. C*, 2008, **112**, 19324–19328.
65 D. H. Xu and W. Z. Shen, *J. Phys. Chem. C*, 2012, **116**, 13368–13373.
66 C. R. Vestal and Z. J. Zhang, *J. Am. Chem. Soc.*, 2003, **125**, 9828–9833.
67 A.-H. Lu, E. L. Salabas and F. Schüth, *Angew. Chem., Int. Ed.*, 2007, **46**, 1222–1244.
68 X. Li, K. Lv, K. Deng, J. Tang, R. Su, J. Sun and L. Chen, *Mater. Sci. Eng., B*, 2009, **158**, 40–47.
69 K. Lv and Y. Xu, *J. Phys. Chem. B*, 2006, **110**, 6204–6212.
70 Y. Xu and C. H. Langford, *Langmuir*, 2001, **17**, 897–902.
71 Y. Xu, K. Lv, Z. Xiong, W. Leng, W. Du, D. Liu and X. Xue, *J. Phys. Chem. C*, 2007, **111**, 19024–19032.
72 C. Yogi, K. Kojima, N. Wada, H. Tokumoto, T. Takai, T. Mizoguchi and H. Tamiaki, *Thin Solid Films*, 2008, **516**, 5881–5884.
73 A. Mills and J. Wang, *J. Photochem. Photobiol., A*, 1999, **127**, 123–134.
74 G. Panthi, A. Yousef, N. A. M. Barakat, K. Abdelrazek Khalil, S. Akhter, Y. Ri Choi and H. Y. Kim, *Ceram. Int.*, 2013, **39**, 2239–2246.
75 S. Gnanam and V. Rajendran, *J. Alloys Compd.*, 2013, **550**, 463–470.
76 M. M. Mohamed, I. Othman and R. M. Mohamed, *J. Photochem. Photobiol., A*, 2007, **191**, 153–161.
77 D. Spuhler, J. Andrés Rengifo-Herrera and C. Pulgarin, *Appl. Catal., B*, 2010, **96**, 126–141.
78 I. Yamazaki and L. H. Piette, *J. Biol. Chem.*, 1990, **265**, 13589–13594.
79 T. Ochiai, H. Nanba, T. Nakagawa, K. Masuko, K. Nakata, T. Murakami, R. Nakano, M. Hara, Y. Koide, T. Suzuki, M. Ikekita, Y. Morito and A. Fujishima, *Catal. Sci. Technol.*, 2012, **2**, 76–78.
80 X. Z. Li, F. B. Li, C. M. Fan and Y. P. Sun, *Water Res.*, 2002, **36**, 2215–2224.